JGR Planets

RESEARCH ARTICLE
10.1029/2020JE006796

The Phase of Water Ice Which Forms in Cold Clouds in the Mesospheres of Mars, Venus, and Earth

T. P. Mangan[1], J. M. C. Plane[1], and B. J. Murray[2]

[1]School of Chemistry, University of Leeds, Leeds, UK, [2]School of Earth and Environment, University of Leeds, Leeds, UK

Key Points:

- Low density amorphous ice was formed at 88–120 K, stacking disordered ice I formed from 121 to 135 K and hexagonal ice I formed at 140–145 K
- Direct deposition results in the stable hexagonal phase at much lower temperatures than when warming stacking disordered ice
- All three phases of ice are possible in clouds in the mesospheres of Earth and Mars, while on Venus only amorphous ice is likely to form

Correspondence to:
B. J. Murray,
B.J.Murray@leeds.ac.uk

Citation:
Mangan, T. P., Plane, J. M. C., & Murray, B. J. (2021). The phase of water ice which forms in cold clouds in the mesospheres of Mars, Venus, and Earth. *Journal of Geophysical Research: Planets*, *126*, e2020JE006796. https://doi.org/10.1029/2020JE006796

Received 4 DEC 2020
Accepted 19 FEB 2021

Author Contributions:
Conceptualization: T. P. Mangan, J. M. C. Plane, B. J. Murray
Data curation: T. P. Mangan
Formal analysis: T. P. Mangan
Investigation: T. P. Mangan, J. M. C. Plane, B. J. Murray
Methodology: T. P. Mangan, J. M. C. Plane, B. J. Murray
Resources: J. M. C. Plane, B. J. Murray
Supervision: J. M. C. Plane, B. J. Murray
Writing – original draft: T. P. Mangan
Writing – review & editing: T. P. Mangan, J. M. C. Plane, B. J. Murray

Abstract Water ice clouds form in the mesospheres of terrestrial planets in the solar system (and most likely elsewhere) by vapor deposition at low pressures and temperatures. Under these conditions a range of crystalline and amorphous phases of ice might form. The phase is important because it influences nucleation kinetics, density, vapor pressure over the solid, growth rates and particle shape. In the past, the temperature range over which these different phases exist has been defined on the basis of depositing ice at low temperature and warming it while observing phase changes. However, the direct deposition of ice at a range of temperatures relevant for the terrestrial planets has not been systematically investigated. Here we present X-ray Diffraction (XRD) measurements of water ice deposited at temperature intervals between 88 and 145 K in a vacuum chamber. XRD patterns showed that low density amorphous ice was formed at ≤120 K, stacking disordered ice I formed from 121 to 135 K and hexagonal ice I formed at 140 and 145 K. Direct deposition results in the stable hexagonal phase at much lower temperatures than when warming stacking disordered ice. All three phases of water ice observed here are possible in clouds in the mesospheres of Earth and Mars, while on Venus only amorphous ice is likely to form.

Plain Language Summary Ice clouds made up of water ice crystals can form in the thin upper atmospheres (mesospheres) of terrestrial planets where it can be extremely cold. Under these conditions a range of crystalline (hexagonal, cubic, or stacking disordered) and amorphous (lacking long range order) phases of ice might form. The phase is important because it influences a range of cloud properties. Experimentally, rather than warming ice formed at low temperature (as has been done in the past) we deposit the ice directly. We did this because an understanding of how the structure of ice evolves on warming as well as what structure forms when ice is deposited at specific temperatures is necessary to understand the properties of these clouds. Measurements showed that the amorphous, stacking disordered and hexagonal phases of water ice (ice I) can form depending on the specific temperature. Direct deposition yields the hexagonal phase at much lower temperatures than when warming ice deposited at lower temperatures. All three phases of water ice observed here are possible in clouds in the mesospheres of Earth and Mars. In contrast, on Venus clouds form at lower temperatures and so only amorphous ice is likely to form.

1. Introduction

Water ice clouds can form in the coldest regions of rarefied planetary upper atmospheres, where particles grow through deposition from the vapor phase. Despite the very low partial pressures of water in the upper atmospheres of Venus, Earth, and Mars, the temperatures can be low enough (~<150 K, depending on the planet) to lead to large supersaturations and the formation of ice particles. At these temperatures multiple metastable forms of ice can exist, but the phases that can form remain poorly defined. In this study, we focus on understanding the phase of ice that forms in this class of very cold clouds which exist in the upper atmospheres of three of the terrestrial planets in the solar system.

In Earth's upper mesosphere (80–90 km), nanoparticles composed primarily of water ice form between 100 and 150 K, producing clouds known as Polar Mesospheric Clouds (PMCs) or noctilucent clouds (NLCs) (Hervig et al., 2001; Rapp & Thomas, 2006; Thomas, 1991). In the Martian atmosphere, water ice clouds have also been observed planet wide at altitudes up to 90 km where temperatures can drop to <120 K (Fedorova et al., 2020; Forget et al., 2009; Vincendon et al., 2011). In addition, water ice particles may serve as seeds for CO_2 ice particles in the Martian mesosphere (Plane et al., 2018). On Venus, the possibility of water

ice clouds has been hypothesized by Turco et al. (1983). At the mesopause (~120 km) temperatures can drop below 100 K, leading to supersaturated conditions conducive for ice particle formation (Chamberlain et al., 2020; Mahieux et al., 2015). Icy grains containing H_2O are also present in the Inter-Stellar Medium (ISM) and past the frost line within the solar system, where it is cold enough (≤150 K) for μm-sized ice particles to form (D'Angelo & Podolak, 2015; Gillett & Forrest, 1973). Examples of temperature profiles for Earth, Mars, and Venus, with calculated saturation ratios with respect to hexagonal ice I are shown in Figure 1. Super-saturated regions with respect to water ice are apparent in the mesospheres of all three planets, with temperatures where $S \geq 1$ ranging from ~140 K down to <80 K.

In the case of PMCs on Earth, the prevailing view is that ice particles are predominantly crystalline ice I based on satellite observations, but the specific crystalline phase is undetermined (Hervig & Gordley, 2010). However, the transitory presence of low-density amorphous (LDA) ice should not be ruled out. LDA ice may nucleate homogeneously depending on the temperature and supersaturation, but may rapidly transition to a crystalline phase (Murray & Jensen, 2010). Also, it has been proposed that the initial phase that would nucleate in PMCs is always LDA ice irrespective of the nucleation mechanism (Nachbar et al., 2018b). Crystallization timescales at different temperatures for this LDA ice then become important for the evolution of cloud particles under these low temperature conditions (Jenniskens & Blake, 1996). For Martian and Venusian mesospheric clouds the temperature minima are generally more extreme than the mesopause on Earth and the phase of ice which forms has not been considered in the literature.

In total, water ice is known to exist in 18 distinct polymorphs, as well as low and high density amorphous forms (del Rosso et al., 2016; Falenty et al., 2014; Loerting et al., 2011; Millot et al., 2018; Salzmann et al., 2011). Under the low temperature and pressure conditions in planetary upper atmospheres, ice I is the only crystalline phase expected to form. Historically, ice I was thought to exist as hexagonal ice (ice I_h) or cubic ice (ice I_c) polymorphs (Hobbs, 1974), however it has become apparent that most samples of ice identified as being cubic were actually made of ice consisting of interlaced layers of cubic and hexagonal sequences, known as stacking disordered ice (ice I_{sd}) which has trigonal symmetry (Hansen et al., 2008; Hobbs, 1974; Kuhs et al., 2012; Malkin et al., 2012, 2015; Salzmann & Murray, 2020). It was only very recently that true ice I_c has been made (del Rosso et al., 2020; Komatsu et al., 2020; Salzmann & Murray, 2020), but the synthesis routes were not relevant for atmospheric ice formation. Both ice I_h and I_c structures are made up of honeycomb layers of hydrogen bonded water molecules, structural differences arise due to the way these layers are arranged. For ice I_h, each layer is a mirror image of the last, for ice I_c each layer is shifted, while a mixture of both stacking sequences leads to ice I_{sd}.

The specific phase formed in these clouds is important as it influences the properties of the particles that form, including the nucleation kinetics, density, vapor pressure over the solid, growth rates, and particle shape. These factors then impact the growth and sedimentation of the ice particles, a process which redistributes water vapor, resulting in a layer with depleted water mixing ratio and below that a layer of enhanced water vapor where the particles sublime (Hervig et al., 2015). In Earth's mesosphere this is thought to alter odd hydrogen and oxygen chemistry (Murray & Plane, 2003; 2005a), and particle phase may also influence the heterogeneous chemistry on mesospheric ice particles (Mangan, Frankland, et al., 2017; Murray & Plane, 2005b; Plane et al., 2004). Similar processes and interactions may occur in the atmospheres of Venus and Mars. Both the boundary between amorphous and crystalline ice formation, and the specific crystal structure of ice formed, is of interest. All of this suggests a complex range of possibilities for the form of ice I, and how much LDA ice is present in planetary upper atmospheres, both of which may depend on factors including deposition temperature, particle warming, saturation ratio, and pressure.

Previous experimental studies of the crystal structure of ice I below 200 K have typically deposited the ice at a single base temperature and observed structural changes via warming (Kuhs et al., 2012; Murray, Malkin, & Salzmann, 2015; Shilling et al., 2006). Indeed, the amorphous to crystalline boundary has primarily been investigated this way, in terms of the transition, rather than determining the temperature at which the ice is no longer amorphous at deposition (Jenniskens & Blake, 1994, 1996; Smith et al., 1996). In contrast, in the present study we use X-ray Diffraction (XRD) to investigate the effect of changing initial deposition temperature on the crystal structure of ice I between 88 and 145 K by vapor depositing ice at regular temperature intervals.

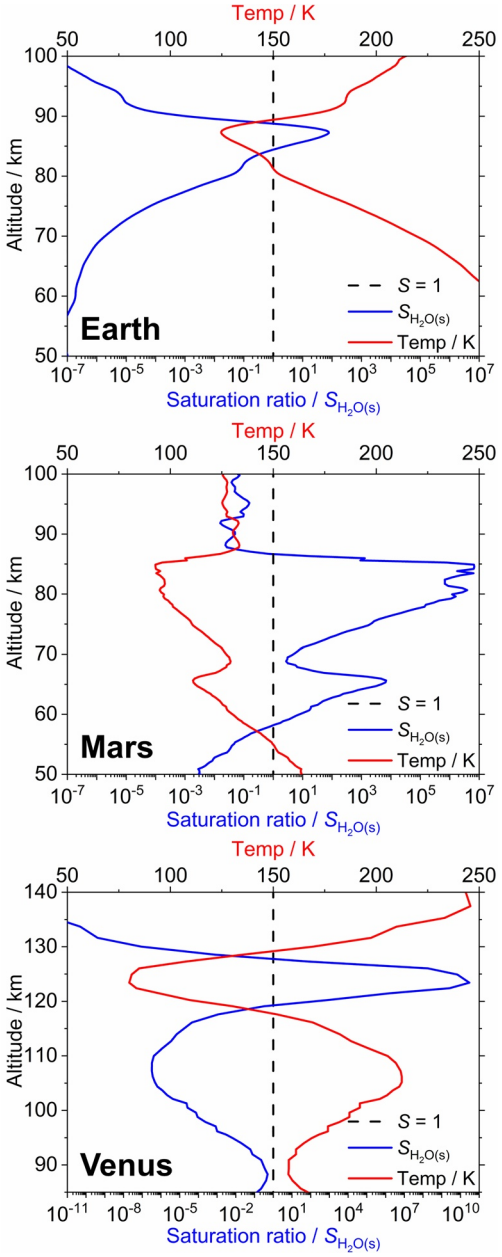

Figure 1. Example temperature profiles and saturation ratios for H_2O ice in the upper atmospheres of Earth, Mars, and Venus. Saturation is defined using H_2O vapor mixing ratios of 5 ppm (Earth), 0.7 ppm (Mars), and 2 ppm (Venus) (Chamberlain et al., 2020; Forget et al., 1999; Hervig et al., 2009). Saturation ratios were calculated using the Nachbar et al. (2019) amorphous correction to the vapor pressure over ice I_h (Murphy & Koop, 2005). The atmospheric profile for Earth was taken from the Solar Occultation for Ice Experiment (SOFIE) database (http://sofie.gats-inc.com), event profile 56463 (Marshall et al., 2011); for Mars, the Mars Pathfinder entry profile (Magalhães et al., 1999); and for Venus, an averaged profile at 70–80° Lat (Mahieux et al., 2012).

2. Methods

To investigate the crystal structure of H_2O under different deposition conditions, we used a temperature-controlled stage within a vacuum chamber, probed using the powder XRD technique which we have employed previously to study deposition of H_2O ice (Murray, Malkin, & Salzmann, 2015; Shilling et al., 2006). Shown in Figure 2, the experimental system described briefly below is in the same configuration as described in Mangan, Salzmann, et al. (2017) for CO_2 deposition, with some modifications to allow for H_2O vapor deposition.

The X-Ray diffractometer (Bruker D8 Advance) was configured in a standard reflectance geometry and equipped with a Cu K-α X-ray source (λ = 1.540598 Å). Diffracted X-rays from a sample mounted on an Anton Paar TTK 450 temperature-controlled stage were detected by a VÅNTEC detector (shown in Figure 2). The TTK 450 chamber was pumped by a Pfeiffer Duo 2.5 A vacuum pump allowing a pressure range of 1×10^{-3}–1×10^{3} mbar. The stage was cooled with liquid nitrogen to temperatures down to 88 ± 0.2 K, measured using a Pt-100 probe inserted into the sample support. The temperature was controlled using a Eurotherm PID controller and resistive heaters. The aluminum sample support was covered with a borosilicate glass slide (160 μm thickness) adhered using a thin layer of vacuum grease.

For each experiment the environmental chamber was first pumped to a pressure of $<1 \times 10^{-2}$ mbar. The sample support was then cooled from room temperature at a rate of 20 K min^{-1} to the specific deposition temperature (110–145 K at deposition temperature increments of 5 K, one experiment at 88 K, as well as 1 K increments around 120 K). At the deposition temperature a diffraction pattern was recorded (2θ = 20–50°, where 2θ is the angle between the transmitted and reflected X-ray beams) before water vapor was introduced, to ensure no ice frosting had occurred on the glass slide. Water vapor was produced by flowing dry N_2 (10 sccm) through two bubblers containing deionized water cooled to 278 K. This wet flow was combined downstream of the bubblers with a dry N_2 flow of 290 sccm, before entering the front of the chamber via a needle valve, with a stable total chamber pressure in each experiment of 10 mbar (20 mbar at 88 K) maintained by throttling the vacuum pump. Low resolution, 30 s scans at 2θ = 22–30° were taken during 20 min of ice growth to monitor the signal (examples at 121 K are shown in Figure 3). The humid N_2 flow was then stopped and a high resolution XRD pattern (5-min scan) with increments of 2θ = 0.0426 for 2θ = 20–50° measured. 2θ values were corrected against a silicon standard, accounting for peak shifting due to sample height.

3. Results

Figure 4 shows the background corrected diffraction patterns of water ice grown for 20 min and deposited at intervals from 88 to 145 K at 10 mbar (88 K measurement taken at 20 mbar) compared with calculated patterns for ice I_{sd}, I_h, and I_c. The diffraction patterns at 110, 115, and 120 K show an absence of defined Bragg peaks with two broad amorphous features. The first, centered around 24° and a broader, weaker feature at >35° centered around 40–45°, are consistent with LDA ice (Dowell & Rinfret, 1960; Shilling et al., 2006). The diffraction pattern taken at 88 K 2θ = 22–30° also shows the broad feature centered at 24°, suggesting LDA ice is deposited from 88 to 120 K.

In order to probe the specific conditions at which the deposited ice is no longer amorphous, experiments were undertaken at 1 K intervals, over a smaller temperature range (119–122 K), shown in Figure 5. The presence of crystalline ice, with defined sharp Bragg peaks is seen consistently in diffraction patterns of

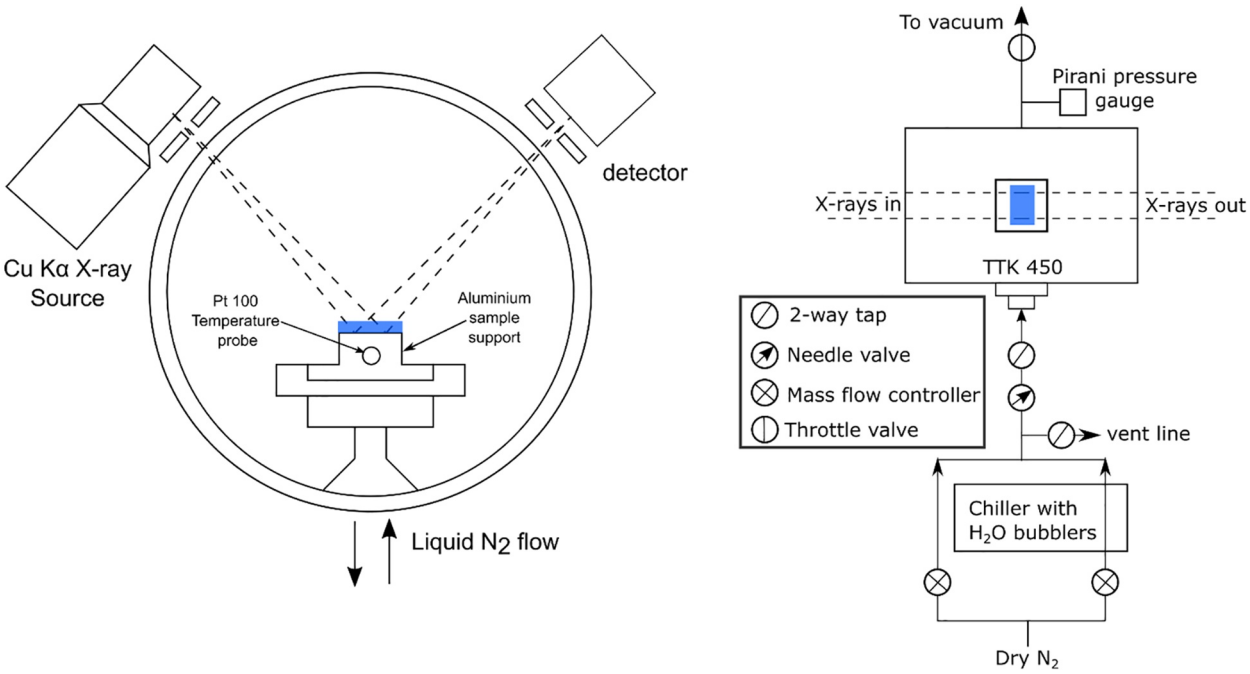

Figure 2. Diagrams of the experimental set-up, including: a front on view of the vacuum chamber with temperature-controlled stage (TTK 450), detector and X-ray source (left), top down view of the experiment including the H_2O vapor flow system (right).

ice deposited at 121 K and above. The experimental peak positions at 24°, 40°, and 48° are consistent with the simulated patterns of I_c and ice I_h. The shoulder peak at 23° is consistent with ice I_h, but the remaining prominent ice I_h peaks are missing (26°, 33.5°, and 44°). Combining these inconsistencies with the feature from 23 to 26° shows that neither pure ice I_h or I_c formed at 121–135 K and instead the crystalline ice formed is consistent with ice I_{sd}. Ice I_{sd} can have a range of cubicities and memory in the stacking sequences (Malkin et al., 2015; Salzmann & Murray, 2020), and we come back to the nature of the ice I_{sd} below.

The experiments at 140 and 145 K show marked differences from the ice I_{sd} deposited at 120–135 K. First, the 40° and 23° peaks are no longer present and neither is the broad feature from 23 to 26° suggesting the ice formed is no longer ice I_{sd}. At 140 K, only two main peaks are present: a high intensity 24° peak (consistent with ice I_h and I_c) and a weaker intensity 43° peak (only seen in the simulated pattern for ice I_h). The absence of stacking disordered features and a peak in the diffraction pattern at 2θ that is only found in ice I_h leads to the conclusion that at 140 K the ice formed is ice I_h, growing with strong preferred crystallographic orientation (we explain this below) rather than ice I_c or I_{sd}. Further evidence for pure ice I_h forming can be found in the ice deposited at 145 K, where two additional small Bragg peaks appear at 26° and 33.5° that are only found in ice I_h. These findings on the structure of ice I with deposition temperature are discussed in the context of the literature in the following section.

The relative intensities of the patterns of crystalline ice are a poor match to the ideal simulated patterns because the samples exhibit preferred crystallographic orientation. The simulated patterns are derived assuming a large population of randomly orientated crystallites are present. However, in our XRD experiments this is not the case and the vapor deposited ice shows evidence of varying degrees of preferred orientation. This occurs because of ordering of the crystallites via oriented growth on the sample surface. In the case of the diffraction patterns shown here, the crystallites are partially ordered, leading to varying intensities of the Bragg peaks for ice I_{sd} and in the case of ice I_h, missing peaks relative to the simulated pattern. For example, in the case of ice I_h at 140 and 145 K the stronger intensity of the 24° peak (associated with the (001) family of faces) suggests that the crystal orientation in these experiments is favoring the basal face growing perpendicular to the incoming X-ray beam.

The strong preferred orientation precludes detailed analysis of the cubicities and stacking probabilities in the ice I_{sd} samples deposited at 130 and 135 K. But, the preferred orientation in the sample deposited at

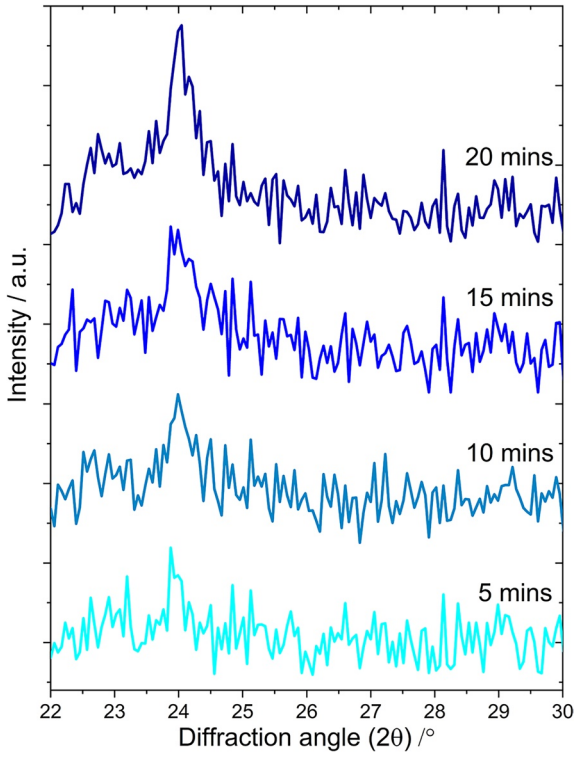

Figure 3. XRD patterns of ice growth at 121 K monitored over 20 min at $2\theta = 22–30°$. The patterns are offset for clarity. XRD, X-ray Diffraction.

125 K is less extreme and we have used the DIFFaX (v1.813) program to tentatively estimate the cubicity of this ice, as has been done previously (Malkin et al., 2012, 2015; Treacy et al., 1991). We have neglected any memory effects in the stacking sequences because the quality of the data is not sufficient to fit this level of detail. With the caveat that there is preferred orientation, we estimate that the probability of finding a cubic sequence is 70% and the corresponding probability of a hexagonal sequence is 30%. This produces a cubicity of 70% at 125 K (the resulting pattern is shown in Figure 4). This cubicity is one of the highest reported for a range of routes to ice I_{sd} (Playford et al., 2018). In contrast Ice I_{sd} made by freezing pure water droplets has a cubicity of 50% with completely random arrangement of cubic and hexagonal sequences (Malkin et al., 2012).

4. Discussion

4.1. The Amorphous—Stacking Disordered Boundary at 120 K

In this study we observe LDA ice at deposition temperatures of ≤120 K while ice I_{sd} is formed at 121–135 K. The formation of LDA ice at the coldest deposition conditions investigated here is consistent with other studies looking at very low temperature ice (Dowell & Rinfret, 1960; Hobbs, 1974; Jenniskens & Blake, 1994). Also, the observation in this study that ice I_{sd} is the coldest observed crystalline form of ice I formed by direct vapor deposition is consistent with other literature, whether the ice was produced by direct vapor deposition or via warmed LDA ice. Using a similar experimental setup, Murray, Malkin and Salzmann (2015) warmed amorphous ice at 1 K min^{-1} from 110 K and observed crystallization to ice I_{sd} at 120 K. However, this crystallization behavior in warmed ice is often seen at temperatures much higher than 120 K. For example, in Jenniskens and Blake (1994), the transition from amorphous to crystalline ice was gradual, where warming at 1–2 K min^{-1} caused changes in diffraction patterns at 131 K. In another example, Hallbrucker et al. (1989) observed a structural relaxation at 136 ± 1 K prior to the onset of crystallization in amorphous ice generated via hyper-quenching water. In other studies, complete crystallization upon warming was not observed until 150–160 K (Jenniskens & Blake, 1994; Johari et al., 1991; Mitlin & Leung, 2004; Shilling et al., 2006; Smith et al., 1996).

The gradual transition to crystalline ice observed in the literature is in stark contrast to what is observed in Figure 5, where the diffraction patterns of ice deposition at ≥121 K show a completely crystalline structure with defined Bragg peaks. Outside of the features associated with ice I_{sd}, the diffraction patterns show no evidence of the broad features associated with amorphous ice. Hobbs (1974) provides a summary of the early experimental research into ice I at low temperatures, covering 16 studies highlighting that the amorphous-crystalline boundary was observed to start and complete over a wide range of temperatures (approximately 110–160 K). However, at least some of these diffraction studies may have misinterpreted the broad feature between 23 and 26° in ice I_{sd} as evidence for the persistence of amorphous ice to relatively high temperatures (Dowell & Rinfret, 1960). Hence, we suggest that the phase transition temperatures reported in some of these earlier studies may not always be reliable.

In a study of the vapor pressure of low temperature ice I, Nachbar et al. (2018a) concluded that because the same nano-crystalline ice polymorph was observed both by warming of amorphous ice and direct vapor deposition, amorphous ice is the initial phase formed by vapor deposition below 160 K before crystallization occurs above 130 K. Crystallization timescales could play a part in the temperature dependent behavior of deposited ice and are an important variable atmospherically. The higher in temperature the amorphous ice is, the quicker crystallization occurs (Dowell & Rinfret, 1960; Jenniskens & Blake, 1996). Isothermal experiments by Jenniskens and Blake (1996) showed amorphous ice warmed to and then held at 125 K took ~5,000 s to show evidence of crystallinity in the diffraction patterns. In contrast, in our study there was a maximum crystallization timescale of about 1800 s and we observe crystalline ice deposited at this temperature. In the present study evidence of defined Bragg peaks associated with crystalline ice are present

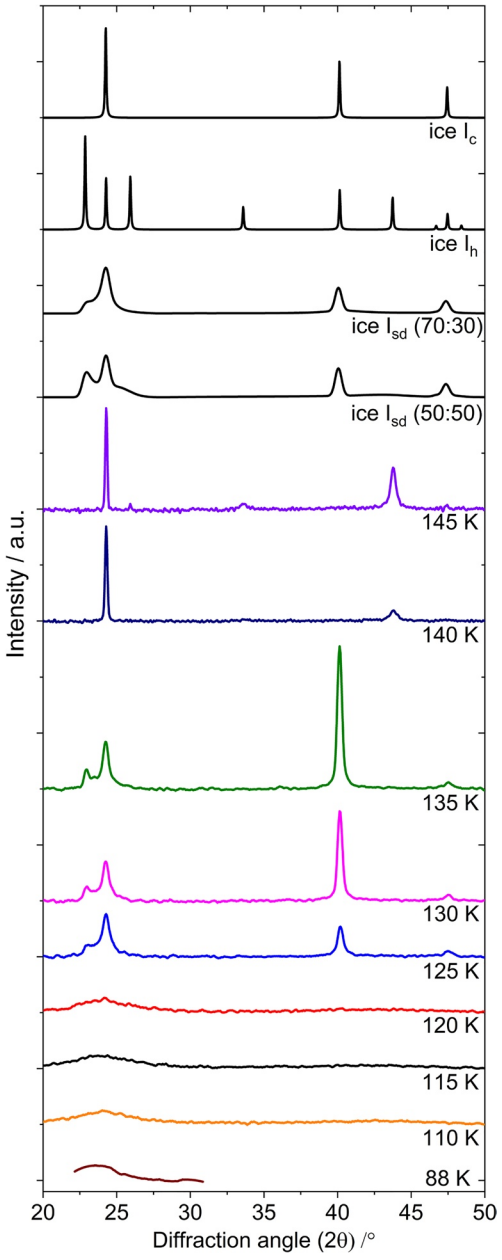

Figure 4. XRD patterns of H_2O ice, vapor deposited at temperatures from 88 to 145 K. Included at the top of the figure are predicted patterns of ice I_h, I_c, and I_{sd} (calculated using DIFFaX v1.813 for 50:50 and 70:30 probabilities of ice I_c and I_h sequences). A summary of the experimental conditions is shown in Table 1. The patterns are offset for clarity. XRD, X-ray Diffraction.

in the first scans taken only 300 s from the onset of deposition at 121 K (shown in Figure 3), while crystallization timescales are several days at this temperature according to Jenniskens and Blake (1996). If amorphous ice forms first then it must have crystallized on timescales shorter than were observable in this experiment, in contrast to slower crystallization in annealed ice from other studies.

4.2. The Deposition of Ice I_h at Relatively Low Temperatures

A striking observation in our study was the very low temperature (140–145 K) at which deposition produced ice I_h, as shown in Figure 4. This result contrasts with the results of a number of previous studies: amorphous ice warmed from the deposition temperature of 110 K by Murray, Malkin and Salzmann (2015) was found to be ice I_{sd} from 120 K all the way up to the highest temperature measured (160 K). In neutron diffraction experiments of annealed ice deposited initially under liq N_2 temperatures, Kuhs et al. (2012) showed that the ice was stacking disordered up to the 175–190 K range. A fraction of cubicity was still apparent during isothermal experiments over the course of 12 h, especially at the lowest (175 K) temperature studied. While LDA ice warmed from 90 K by Shilling et al. (2006) was still in the form ice I_{sd} at 180 K and persisted for at least 60 min. The literature review in Hobbs (1974) shows that ice I_h is typically observed from ~170 to 200 K. Experiments by Dowell and Rinfret (1960) suggested conversion to ice I_h occurs at ≥ 140 K. However, there is a caveat in that these early studies were carried out before stacking disorder in ice I was recognised. It appears from the discussion in Dowell and Rinfret (1960) that the peak at ~23° was interpreted as evidence for ice I_h, but we now know that this peak is consistent with ice I_{sd} (Malkin et al., 2015). In addition, the broad feature of ice I_{sd} centered around 23-26° in combination with sharp diffraction peaks has in the past been interpreted as amorphous ice mixed with ice I_h and ice I_c (Dowell & Rinfret, 1960; Kohl et al., 2000). These features have now clearly been shown to be related to stacking disorder (Malkin et al., 2012, 2015). Overall, these literature studies suggest that ice I_{sd} persists to temperatures as high as 190 K, in strong contrast to our study where we deposited directly. To verify that our experimental system was not promoting ice I_h, we deposited LDA ice at 110 K and warmed it to 160 K (see Figure 6). The ice at 160 K was ice I_{sd}, fitted using DIFFaX v1.813 (with the same caveats as the fitting of the 125 K experiment) with a 65:35 probability of ice I_c and I_h sequences (65% cubicity). Crystallization here to ice I_{sd} upon warming amorphous ice is similar to the findings of Murray, Malkin and Salzmann (2015) and the other studies listed above. Hence there does appear to be a strong difference between the ice phase produced through direct deposition and that of ice deposited at low temperatures and warmed.

The effect of saturation ratio (and therefore growth rate) on the formation of ice is an experimentally and atmospherically relevant variable that could influence which polymorph of ice I is produced. In this study the flow of water vapor and the chamber pressure was fixed, leading to higher saturation ratios with respect to the solid phase at the lower temperatures (Table 1: at 145 K the saturation ratio ($S_{LDA\ ice}$) is ~3×10^4 while at 110 K it is ~1×10^{10}). Hudait and Molinero (2016) grew ice I between 200 to 260 K in a modeling study and concluded that the crystal structure was linked to growth rate and therefore also linked to saturation ratio. Ices formed at higher saturation ratios (>1.6×10^4) were found to form ice I_{sd}, with ice I_h forming at lower saturation ratios. This trend in saturation although not directly comparable is consistent with the data observed here, where the highest temperatures (140–145 K) and lowest saturation ratios (~$(0.3–1) \times 10^5$) leads to ice I_h formation. This may also

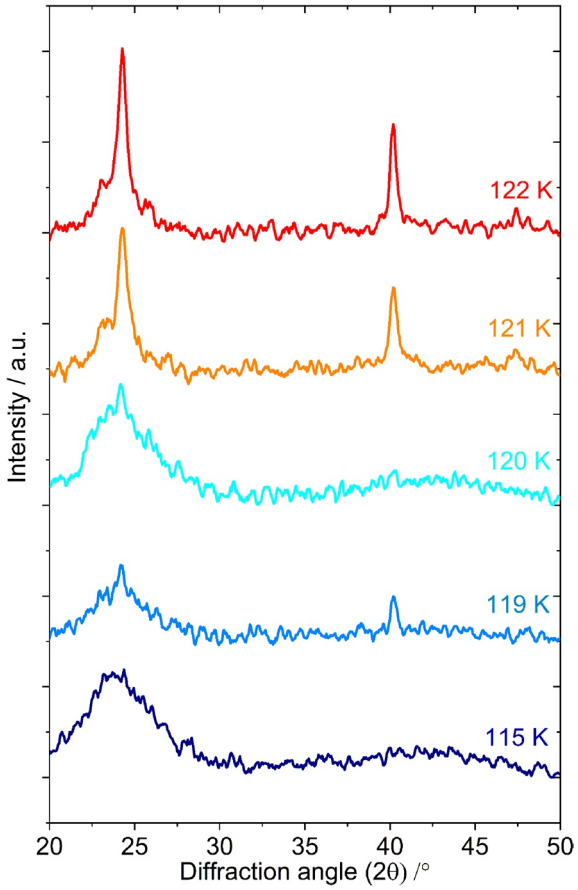

Figure 5. XRD patterns of vapor deposited ice close to the amorphous-crystalline boundary of ice I at 115–122 K. The patterns are offset for clarity. XRD, X-ray Diffraction.

be the situation in planetary atmospheres where supersaturation is driven primarily by temperature with relatively constant water mixing ratio.

We now turn to why ice I_h is favored when deposited at and above 140 K, whereas ice I_{sd} is favored at these temperatures when ice is deposited at lower temperatures and warmed. This issue is related to the fact that ice I_{sd} is favored when ice is grown from liquid water. Hudait and Molinero (2016) concluded that there is a significant surface energy cost of ice I_{sd} over ice I_h. In fact, the energy cost against cubic ice sequences at the ice-vapor interface is about 25 times greater than that in the ice-liquid interface (Hudait & Molinero, 2016; Hudait et al., 2016). This means that when ice grows from the vapor, there is a strong thermodynamic driver for any cubic sequences to relax to the hexagonal configuration. This is only overcome at relatively high growth rates (at high supersaturation) where the cubic sequences are buried in the ice structure before they get a chance to relax to the more stable hexagonal configuration. Similarly, when ice grows from an aqueous environment, the growth is rapid relative to reorganisation, locking the ice in the kinetic product, that is ice I_{sd} (Malkin et al., 2015). Ice I_{sd} is apparent in diffraction patterns of liquid droplets deposited down to 130 K (Kohl et al., 2000). This also offers an insight into why ice I_{sd} is produced at temperatures ≤135 K and persists when warmed to higher temperatures. At low temperatures ice I_{sd} is favored in part because the rate of reorganisation at the surface slows with decreasing temperature, but also because the supersaturation and growth rate increases for a given mixing ratio of water vapor (Hudait & Molinero, 2016). The metastable cubic sequences are then locked within the "bulk" ice, so when the ice is warmed, the stacking disorder persists until the vapor transport route becomes relatively rapid (on an hour-minute time scale) at temperatures above ~190 K (Murphy, 2003). It has been suggested in the past that ice I_{sd} crystals might grow in cirrus clouds in the Earth's Tropical Tropopause Layer (TTL) (180–200 K) (Kuhs et al., 2012; Murray et al., 2005), but our results suggest that even if aqueous droplets freeze to ice I_{sd}, subsequent growth will result in ice I_h. This finding is consistent with the molecular simulations by Hudait and Molinero (2016), although some stacking faults in predominantly hexagonal structures might be possible, and would be consistent with observed trigonal symmetry in some ice crystals (Kuhs et al., 2012; Murray, Salzmann, et al., 2015).

5. Implications for Clouds in Planetary Mesospheres

The experimental results presented in this study suggest that deposition of LDA ice, ice I_{sd} and ice I_h may be possible across just a 20 K temperature range, with implications for the crystal phase present in these clouds. It should be noted, as discussed in the previous section, that a range of temperatures have been reported for each ice I phase in the literature, and so a range of conditions for each may be possible atmospherically.

A comparison of the super-saturated regions (regions kinetically favorable for stable ice crystals with $S \geq 1$) are shown in Figure 1 for the upper atmospheres of Earth, Mars, and Venus at fixed water vapor mixing ratios (see the figure caption for values). It is worth noting that super-saturation is exponentially dependent on temperature and only linearly dependent on the water vapor mixing ratio, making temperature the key driver. The implications of the experimental results presented here are discussed for water ice clouds on each planet.

5.1. Earth

The temperature profile shown for Earth in Figure 1 is a satellite measurement from June 30, 2012 at 67°N, which represents a typical cold profile seen during the northern hemisphere PMC season occurring between late May and late August. In the mesosphere of Earth, the temperature range where $S \geq 1$ for the pro-

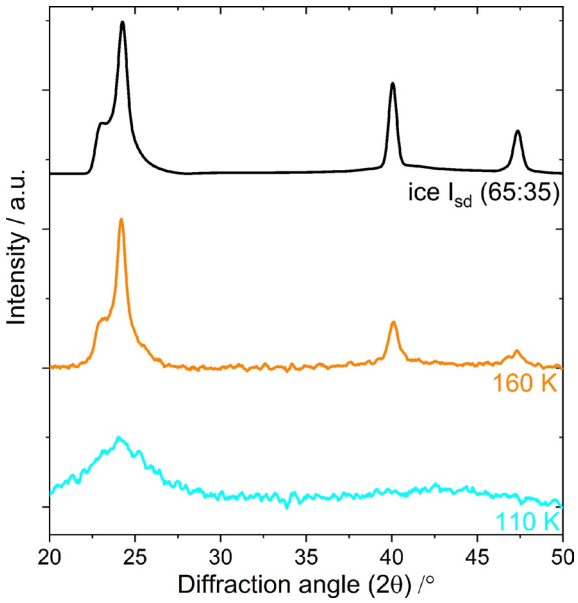

Figure 6. XRD patterns of H_2O ice, vapor deposited at 110 K and then warmed to 160 K. Included at the top of the figure is a predicted pattern for stacking disordered ice, ice I_{sd} (calculated using DIFFaX v1.813 for a 65:35 probability of ice I_c and I_h sequences). The patterns are offset for clarity. XRD, X-ray Diffraction.

file shown is approximately 125–140 K at 84–88 km altitude, around the mesopause altitude. Generally, PMC ice particle temperatures exist in the range of 120–150 K (Hervig & Gordley, 2010). PMCs which scatter enough light to be optically visible tend to occur several km below the cold point of the mesopause (when they can appear as NLCs to a ground-based observer), but ice particles are thought to also exist close to the mesopause as evidenced by the presence of Polar Mesospheric Summer Echoes (PMSEs) (Rapp & Lübken, 2004; Russell III et al., 2010). These ice particles are thought to nucleate near the cold point, and then grow and sediment to form the visible cloud (Rapp & Thomas, 2006; von Zahn & Berger, 2003).

The evidence from this study and others suggests most PMCs that form between 120 and 135 K will be ice I_{sd} crystals. As the ice particles sediment and reach warmer temperatures, the ice I_{sd} structure will likely persist (Murray, Malkin, & Salzmann, 2015). Ice crystals that sediment into regions warmer than ~140 K may then grow through the deposition of ice I_h. At the mesopause, conditions are sometimes cold enough that LDA ice particles can form, as previously suggested (Lübken et al., 2009; Murray & Jensen, 2010). Upon warming these LDA ice particles would likely transition to ice I_{sd} so that LDA ice is probably a transient phase and will not be present in the bulk of PMCs, consistent with previous satellite measurement which indicate crystalline ice dominates PMCs (Hervig & Gordley, 2010). However, LDA ice may be important in the early stages of cloud development. For example, the equilibrium vapor pressure of LDA ice is substantially larger than crystalline ices, hence this may drive a mass transfer process analogous to the Werner-Bergeron-Findeisen process in Earth's tropospheric clouds composed of mixtures of liquid water and ice (Murray et al., 2012; Nachbar et al., 2018b). In this process, a few particles of crystalline ice grow at the expense of LDA particles, potentially leading to a reduced number of hydrometeors of larger size. Overall, it is striking that all three phases of ice may be present and important in the evolution of mesospheric clouds on Earth.

5.2. Mars

For Mars, as can be seen from the Mars Pathfinder entry profile shown in Figure 1, the situation is distinct to that on Earth. A colder temperature profile, with a wide altitude range of extreme cold temperatures leads to a large saturated region ($S \geq 1$ for <135 K at 58–87 km in this profile), one that is significantly more supersaturated than for Earth. Mars lacks a significant ozone layer and a clear mesopause, leading to a much more variable altitude at which the temperature minimum occurs. This temperature minimum is influenced heavily by dynamical processes such as gravity waves causing a much larger range of altitudes (30–90 km) in the atmosphere (especially in the mountainous equatorial regions for solar longitude Ls = ~0–150°) where the coldest water ice clouds are typically observed (Fedorova et al., 2020; Heavens et al., 2020; Vincendon et al., 2011).

Water ice clouds observed in the mesosphere (~80 km) with the strongest temperature minima (~80 K) will likely form as particles of LDA ice which could transform to ice I_{sd} at warmer temperatures, in a similar way to PMCs on Earth. Observations during the dust storm season have highlighted the presence of water ice at altitudes of ~80–90 km at temperatures <150 K, suggesting that ice I_{sd} and ice I_h may also be possible for these warmer mesospheric clouds (Fedorova et al., 2020). Similarly, clouds forming in the lower mesosphere (<60 km) are more likely to lead to ice I_{sd} and possibly ice I_h particle formation depending on the specific conditions. Water ice clouds can also form all the way down to the Mar-

Table 1
Experimental Saturation Ratios for Liquid (S_{liq}), Ice I_h ($S_{ice\ Ih}$), and the LDA Ice Correction to $S_{ice\ Ih}$ ($S_{LDA\ ice}$)

Sample temperature / K	S_{liq} [a]	$S_{ice\ Ih}$ [a]	$S_{LDA\ ice}$ [b]
88	3.09×10^{16}	1.86×10^{17}	9.57×10^{15}
110	2.83×10^{10}	1.11×10^{11}	1.08×10^{10}
115	2.80×10^{9}	1.03×10^{10}	1.11×10^{9}
120	3.35×10^{8}	1.15×10^{9}	1.38×10^{8}
125	4.74×10^{7}	1.54×10^{8}	2.01×10^{7}
130	7.77×10^{6}	2.39×10^{7}	3.41×10^{6}
135	1.45×10^{6}	4.24×10^{6}	6.55×10^{5}
140	3.05×10^{5}	8.51×10^{5}	1.42×10^{5}
145	7.14×10^{4}	1.90×10^{5}	3.39×10^{4}

[a]Murphy and Koop (2005) [b]Nachbar et al. (2019).
Abbreviation: LDA, low-density amorphous.

tian surface (~0–30 km) at temperatures from ~180-215 K, under similar temperature conditions to TTL cirrus on Earth, and so should also form primarily particles of ice I_h (Pankine & Tamppari, 2015; Whiteway et al., 2009; Wilson & Guzewich, 2014).

5.3. Venus

The profile shown in Figure 1 for the Venusian upper atmosphere is taken from the SOIR Instrument onboard the Venus Express satellite in the 70–80° latitude region (Mahieux et al., 2012). A temperature minimum (~80 K) is observed in this profile around an altitude of 125 km, although the temperature can drop as low as 60 K based on other observations (Mahieux et al., 2015). This temperature minimum is often observed around 120–130 km for measurements taken at the terminators, though the extent of the temperature minima is variable. The super-saturated region shown here occurs at temperatures <130 K, over a 119–129 km altitude range. The Venusian mesosphere where ice clouds may form is more rarefied (~10^{-5} Pa) than the coldest regions observed on Earth and Mars (1–10^{-2} Pa), hence much more extreme temperature minima are required for nucleation. It is suggested that if clouds form at these high altitudes they will likely produce small subvisible nanoparticles (Turco et al., 1983). Small particles of water ice forming at ~60–120 K could persist as LDA ice and are unlikely to undergo significant crystallization to ice I_{sd} before sublimation under warmer conditions. The temperatures on Venus are probably too high to form the high density counterpart of LDA ice, HDA ice, which requires vapor deposition below 38 K to form (Jenniskens & Blake, 1994). Given the need for temperatures below 130 K to produce supersaturated air, Venus is the only atmosphere discussed here where ice I_h is unlikely to form and where the dominant phase may be LDA.

5.4. Ice Nucleation and Crystal Shape

It is thought that an amorphous phase is the initial material to nucleate when particles nucleate homogeneously from the vapor, since the nucleation barrier for the formation of an amorphous cluster is smaller than for a crystalline cluster (Huang & Bartell, 1995; Murray & Jensen, 2010). Of particular relevance to planetary mesospheric clouds, Nachbar et al. (2018a) concluded that the initial phase that forms for temperatures <160 K is always LDA ice. Furthermore, an ice activation model using the bulk properties of LDA ice was also able to satisfactorily reproduce heterogeneous ice nucleation experiments at ~140–150 K (Duft et al., 2019). The mesospheric clouds discussed for Earth, Mars, and Venus all form below 150 K, suggesting that at least the nucleation kinetics of ice particles forming by deposition in these atmospheres will be governed by the properties of LDA ice, including associated parameters such as vapor pressure, surface tension, and density. Depending on the temperature, timescale, growth rate and size of the ice particles, the initial amorphous clusters formed below 160 K may transform to ice I_{sd}. If the temperature is low enough (≤120 K) or either growth or particle lifetime is limited, they can instead persist as LDA ice. Hudait and Molinero (2016) suggest that at the high supersaturations possible in experiments and in planetary upper atmospheres (e.g., $S = 10^6$–10^8), crystalline ice I_{sd} is more likely to form than ice I_h. This saturation range is comparable to that seen over the 120–135 K range in this study (1.4×10^8–6.6×10^5) where ice I_{sd} is observed. Precipitation of particles from colder to warmer regions, short-lived perturbations of the temperature profile cause by gravity waves, and the effect of varying supersaturation, provides the possibility of multiple phases being present in these clouds. The phase that grows then determines the possibilities for the overall shape of the crystal.

The lack of long-range order in LDA ice suggests that once the particles grow large enough that the shape is no longer significantly influenced by the addition of a single water molecule (diameter of a H_2O molecule ~0.27 nm), they will be approximately spherical. Crystals with a structure of ice I_{sd} (the likely most abundant crystalline phase in the mesospheric clouds for Earth and Mars) are trigonal, forming columns or plates with aspect ratios larger than spherical particles (Murray, Salzmann, et al., 2015). Crystals of ice I_h will also be anisotropic and will lead to columns and plates, albeit with six-fold symmetry. Ice I_c (which is not expected to form for the clouds discussed here based on experimental evidence), would form more compact isotropic crystals. For PMCs on Earth, the expectation of primarily ice I_{sd} and ice I_h is consistent with observations of high aspect ratio, non-spherical crystals (Hervig & Gordley, 2010; Rapp et al., 2007). For Mars, the elongated crystal shapes of the tropospheric water ice (ice I_h) clouds differentiate them from

CO_2-I ice clouds, which form more compact crystal shapes similar to ice I_c, such as cubes and octahedra (Mangan, Salzmann, et al., 2017).

6. Conclusions

Diffraction patterns of unannealed, vapor deposited water ice at 10 mbar (20 mbar at 88 K) have been presented in this study at temperatures from 88 to 145 K. LDA ice was found to form at deposition temperatures of 88–120 K with a boundary at ~120 K between amorphous and crystalline ice deposition. Ice I_{sd} was deposited at ~120–135 K and ice I_h at 140 and 145 K. LDA ice was also annealed from 110 up to 160 K producing ice I_{sd}, highlighting the difference in crystal structure between ice deposited directly at a particular temperature and ice deposited at lower temperature and then warmed to the same temperature.

The crystal structure of ice I in the mesospheric clouds of Earth, Mars and Venus was inferred from the experiments undertaken in this study. For Earth and Mars conditions should exist for all three phases of ice I to occur, with the predominant structure in mesospheric clouds likely to be ice I_{sd}, and LDA ice under extreme low temperature conditions. In contrast, lower altitude clouds on Earth and Mars are likely to be comprised of ice I_h particles. On Venus, clouds that may form around 125 km would likely be LDA ice. Particles of ice I_{sd} and I_h will form anisotropic crystals, such as needles and plates, while LDA ice should lead to more spherical particles. Overall, the results of this study show that amorphous, metastable stacking disordered and stable hexagonal ice may form and influence the properties of clouds in the mesospheres of terrestrial planets.

Data Availability Statement

The data set for this research can be accessed at Mangan et al. (2021).

Acknowledgments
This work was supported by grant ST/T000279/1 from the UK Science and Technology Facilities Council.

References

Chamberlain, S., Mahieux, A., Robert, S., Piccialli, A., Trompet, L., Vandaele, A. C., & Wilquet, V. (2020). SOIR/VEx observations of water vapor at the terminator in the Venus mesosphere. *Icarus*, *346*, 113819. https://doi.org/10.1016/j.icarus.2020.113819

D'Angelo, G., & Podolak, M. (2015). Capture and evolution of planetesimals in Circumjovian Disks. *The Astrophysical Journal*, *806*(2), 203. https://doi.org/10.1088/0004-637x/806/2/203

del Rosso, L., Celli, M., Grazzi, F., Catti, M., Hansen, T. C., Fortes, A. D., & Ulivi, L. (2020). Cubic ice Ic without stacking defects obtained from ice XVII. *Nature Materials*, *19*(6), 663–668. https://doi.org/10.1038/s41563-020-0606-y

del Rosso, L., Grazzi, F., Celli, M., Colognesi, D., Garcia-Sakai, V., & Ulivi, L. (2016). Refined Structure of metastable ice XVII from neutron diffraction measurements. *The Journal of Physical Chemistry C*, *120*(47), 26955–26959. https://doi.org/10.1021/acs.jpcc.6b10569

Dowell, L. G., & Rinfret, A. P. (1960). Low-temperature forms of ice as studied by X-Ray diffraction. *Nature*, *188*(4757), 1144–1148. https://doi.org/10.1038/1881144a0

Duft, D., Nachbar, M., & Leisner, T. (2019). Unraveling the microphysics of polar mesospheric cloud formation. *Atmospheric Chemistry and Physics*, *19*(5), 2871–2879. https://doi.org/10.5194/acp-19-2871-2019

Falenty, A., Hansen, T. C., & Kuhs, W. F. (2014). Formation and properties of ice XVI obtained by emptying a type sII clathrate hydrate. *Nature*, *516*(7530), 231–233. https://doi.org/10.1038/nature14014

Fedorova, A. A., Montmessin, F., Korablev, O., Luginin, M., Trokhimovskiy, A., Belyaev, D. A., et al. (2020). Stormy water on Mars: The distribution and saturation of atmospheric water during the dusty season. *Science*, *367*, eaay9522. https://doi.org/10.1126/science.aay9522

Forget, F., Hourdin, F., Fournier, R., Hourdin, C., Talagrand, O., Collins, M., et al. (1999). Improved general circulation models of the Martian atmosphere from the surface to above 80 km. *Journal of Geophysical Research*, *104*(E10), 24155–24175. https://doi.org/10.1029/1999je001025

Forget, F., Montmessin, F., Bertaux, J.-L., González-Galindo, F., Lebonnois, S., Quémerais, E., et al. (2009). Density and temperatures of the upper Martian atmosphere measured by stellar occultations with Mars Express SPICAM. *Journal of Geophysical Research*, *114*(E1). https://doi.org/10.1029/2008je003086

Gillett, F. C., & Forrest, W. J. (1973). Spectra of the Becklin-Neugebauer point source and the Kleinmann-Low nebula from 2.8 to 13.5 microns. *The Astrophysical Journal*, *179*, 483. https://doi.org/10.1086/151888

Hallbrucker, A., Mayer, E., & Johari, G. P. (1989). Glass-liquid transition and the enthalpy of devitrification of annealed vapor-deposited amorphous solid water: a comparison with hyperquenched glassy water. *Journal of Physical Chemistry*, *93*(12), 4986–4990. https://doi.org/10.1021/j100349a061

Hansen, T. C., Koza, M. M., & Kuhs, W. F. (2008). Formation and annealing of cubic ice: I. Modeling of stacking faults. *Journal of Physics: Condensed Matter*, *20*(28), 285104. https://doi.org/10.1088/0953-8984/20/28/285104

Heavens, N. G., Kass, D. M., Kleinböhl, A., & Schofield, J. T. (2020). A multiannual record of gravity wave activity in Mars's lower atmosphere from on-planet observations by the Mars Climate Sounder. *Icarus*, *341*, 113630. https://doi.org/10.1016/j.icarus.2020.113630

Hervig, M. E., & Gordley, L. L. (2010). Temperature, shape, and phase of mesospheric ice from Solar Occultation for Ice Experiment observations. *Journal of Geophysical Research*, *115*(D15). https://doi.org/10.1029/2010jd013918

Hervig, M. E., Siskind, D. E., Bailey, S. M., & Russell, J. M. (2015). The influence of PMCs on water vapor and drivers behind PMC variability from SOFIE observations. *Journal of Atmospheric and Solar-Terrestrial Physics*, *132*, 124–134. https://doi.org/10.1016/j.jastp.2015.07.010

Hervig, M. E., Stevens, M. H., Gordley, L. L., Deaver, L. E., Russell, J. M., III, & Bailey, S. M. (2009). Relationships between polar mesospheric clouds, temperature, and water vapor from Solar Occultation for Ice Experiment (SOFIE) observations. *Journal of Geophysical Research*, *114*(D20). https://doi.org/10.1029/2009jd012302

Hervig, M. E., Thompson, R. E., McHugh, M., Gordley, L. L., Russell, J. M., III, & Summers, M. E. (2001). First confirmation that water ice is the primary component of polar mesospheric clouds. *Geophysical Research Letters*, *28*(6), 971–974. https://doi.org/10.1029/2000gl012104

Hobbs, P. V. (1974). *Ice physics*. Oxford, UK: Clarendon Press.

Huang, J., & Bartell, L. S. (1995). Kinetics of homogeneous nucleation in the freezing of large water clusters. *Journal of Physical Chemistry*, *99*(12), 3924–3931. https://doi.org/10.1021/j100012a010

Hudait, A., & Molinero, V. (2016). What determines the ice polymorph in clouds? *Journal of the American Chemical Society*, *138*(28), 8958–8967. https://doi.org/10.1021/jacs.6b05227

Hudait, A., Qiu, S., Lupi, L., & Molinero, V. (2016). Free energy contributions and structural characterization of stacking disordered ices. *Physical Chemistry Chemical Physics*, *18*(14), 9544–9553. https://doi.org/10.1039/C6CP00915H

Jenniskens, P., & Blake, D. F. (1994). Structural transitions in amorphous water ice and astrophysical implications. *Science*, *265*(5173), 753–756. https://doi.org/10.1126/science.11539186

Jenniskens, P., & Blake, D. F. (1996). Crystallization of amorphous water ice in the solar system. *The Astrophysical Journal*, *473*(2), 1104–1113. https://doi.org/10.1086/178220

Johari, G. P., Hallbrucker, A., & Mayer, E. (1991). The dielectric behavior of vapor-deposited amorphous solid water and of its crystalline forms. *The Journal of Chemical Physics*, *95*(4), 2955–2964. https://doi.org/10.1063/1.460897

Kohl, I., Mayer, E., & Hallbrucker, A. (2000). The glassy water–cubic ice system: A comparative study by X-ray diffraction and differential scanning calorimetry. *Physical Chemistry Chemical Physics*, *2*(8), 1579–1586. https://doi.org/10.1039/A908688I

Komatsu, K., Machida, S., Noritake, F., Hattori, T., Sano-Furukawa, A., Yamane, R., et al. (2020). Ice Ic without stacking disorder by evacuating hydrogen from hydrogen hydrate. *Nature Communications*, *11*(1), 464. https://doi.org/10.1038/s41467-020-14346-5

Kuhs, W. F., Sippel, C., Falenty, A., & Hansen, T. C. (2012). Extent and relevance of stacking disorder in "ice I_c". *Proceedings of the National Academy of Sciences*, *109*(52), 21259. https://doi.org/10.1073/pnas.1210331110

Loerting, T., Winkel, K., Seidl, M., Bauer, M., Mitterdorfer, C., Handle, P. H., et al. (2011). How many amorphous ices are there? *Physical Chemistry Chemical Physics*, *13*(19), 8783–8794. https://doi.org/10.1039/C0CP02600J

Lübken, F. J., Lautenbach, J., Hoffner, J., Rapp, M., & Zecha, M. (2009). First continuous temperature measurements within polar mesosphere summer echoes. *Journal of Atmospheric and Solar-Terrestrial Physics*, *71*(3–4), 453–463. https://doi.org/10.1016/j.jastp.2008.06.001

Magalhães, J. A., Schofield, J. T., & Seiff, A. (1999). Results of the Mars Pathfinder atmospheric structure investigation. *Journal of Geophysical Research*, *104*(E4), 8943–8955. https://doi.org/10.1029/1998je900041

Mahieux, A., Vandaele, A. C., Bougher, S. W., Drummond, R., Robert, S., Wilquet, V., et al. (2015). Update of the Venus density and temperature profiles at high altitude measured by SOIR on board Venus Express. *Planetary and Space Science*, *113–114*, 309–320. https://doi.org/10.1016/j.pss.2015.02.002

Mahieux, A., Vandaele, A. C., Robert, S., Wilquet, V., Drummond, R., Montmessin, F., & Bertaux, J. L. (2012). Densities and temperatures in the Venus mesosphere and lower thermosphere retrieved from SOIR on board Venus Express: Carbon dioxide measurements at the Venus terminator. *Journal of Geophysical Research*, *117*(E7). https://doi.org/10.1029/2012je004058

Malkin, T. L., Murray, B. J., Brukhno, A. V., Anwar, J., & Salzmann, C. G. (2012). Structure of ice crystallized from supercooled water. *Proceedings of the National Academy of Sciences*, *109*(4), 1041. https://doi.org/10.1073/pnas.1113059109

Malkin, T. L., Murray, B. J., Salzmann, C. G., Molinero, V., Pickering, S. J., & Whale, T. F. (2015). Stacking disorder in ice I. *Physical Chemistry Chemical Physics*, *17*(1), 60–76. https://doi.org/10.1039/C4CP02893G

Mangan, T. P., Frankland, V. L., Murray, B. J., & Plane, J. M. C. (2017). The fate of meteoric metals in ice particles: Effects of sublimation and energetic particle bombardment. *Journal of Atmospheric and Solar-Terrestrial Physics*, *161*, 143–149. https://doi.org/10.1016/j.jastp.2017.07.002

Mangan, T. P., Plane, J. M. C., & Murray, B. J. (2021). *X ray diffraction patterns for water ice at low pressures between 88-145 K—Dataset*. University of Leeds. https://doi.org/10.5518/946

Mangan, T. P., Salzmann, C. G., Plane, J. M. C., & Murray, B. J. (2017). CO_2 ice structure and density under Martian atmospheric conditions. *Icarus*, *294*, 201–208. https://doi.org/10.1016/j.icarus.2017.03.012

Marshall, B. T., Deaver, L. E., Thompson, R. E., Gordley, L. L., McHugh, M. J., Hervig, M. E., & Russell, J. M., III (2011). Retrieval of temperature and pressure using broadband solar occultation: SOFIE approach and results. *Atmospheric Measurement Techniques*, *4*(5), 893–907. https://doi.org/10.5194/amt-4-893-2011

Millot, M., Hamel, S., Rygg, J. R., Celliers, P. M., Collins, G. W., Coppari, F., et al. (2018). Experimental evidence for superionic water ice using shock compression. *Nature Physics*, *14*(3), 297–302. https://doi.org/10.1038/s41567-017-0017-4

Mitlin, S., & Leung, K. T. (2004). Temporal evolution of an ultrathin, noncrystalline ice deposit at crystallization near 160 K studied by FT-IR reflection-absorption spectroscopy. *Canadian Journal of Chemistry*, *82*(6), 978–986. https://doi.org/10.1139/v04-076

Murphy, D. M. (2003). Dehydration in cold clouds is enhanced by a transition from cubic to hexagonal ice. *Geophysical Research Letters*, *30*(23). https://doi.org/10.1029/2003GL018566

Murphy, D. M., & Koop, T. (2005). Review of the vapor pressures of ice and supercooled water for atmospheric applications. *Quarterly Journal of the Royal Meteorological Society*, *131*(608), 1539–1565. https://doi.org/10.1256/qj.04.94

Murray, B. J., & Jensen, E. J. (2010). Homogeneous nucleation of amorphous solid water particles in the upper mesosphere. *Journal of Atmospheric and Solar-Terrestrial Physics*, *72*(1), 51–61. https://doi.org/10.1016/j.jastp.2009.10.007

Murray, B. J., Knopf, D. A., & Bertram, A. K. (2005). The formation of cubic ice under conditions relevant to Earth's atmosphere. *Nature*, *434*(7030), 202–205. https://doi.org/10.1038/nature03403

Murray, B. J., Malkin, T. L., & Salzmann, C. G. (2015). The crystal structure of ice under mesospheric conditions. *Journal of Atmospheric and Solar-Terrestrial Physics*, *127*, 78–82. https://doi.org/10.1016/j.jastp.2014.12.005

Murray, B. J., O'Sullivan, D., Atkinson, J. D., & Webb, M. E. (2012). Ice nucleation by particles immersed in supercooled cloud droplets. *Chemical Society Reviews*, *41*(19), 6519–6554. https://doi.org/10.1039/C2CS35200A

Murray, B. J., & Plane, J. M. C. (2003). The uptake of atomic oxygen on ice films: Implications for noctilucent clouds. *Physical Chemistry Chemical Physics*, *5*(19), 4129–4138. https://doi.org/10.1039/B305555H

Murray, B. J., & Plane, J. M. C. (2005a). Modeling the impact of noctilucent cloud formation on atomic oxygen and other minor constituents of the summer mesosphere. *Atmospheric Chemistry and Physics*, *5*(4), 1027–1038. https://doi.org/10.5194/acp-5-1027-2005

Murray, B. J., & Plane, J. M. C. (2005b). Uptake of Fe, Na and K atoms on low-temperature ice: implications for metal atom scavenging in the vicinity of polar mesospheric clouds. *Physical Chemistry Chemical Physics*, *7*(23), 3970–3979. https://doi.org/10.1039/B508846A

Murray, B. J., Salzmann, C. G., Heymsfield, A. J., Dobbie, S., Neely, R. R., III, & Cox, C. J. (2015). Trigonal ice crystals in Earth's atmosphere. *Bulletin of the American Meteorological Society*, *96*(9), 1519–1531. https://doi.org/10.1175/BAMS-D-13-00128.1

Nachbar, M., Duft, D., & Leisner, T. (2018a). The vapor pressure over nano-crystalline ice. *Atmospheric Chemistry and Physics*, *18*(5), 3419–3431. https://doi.org/10.5194/acp-18-3419-2018

Nachbar, M., Duft, D., & Leisner, T. (2018b). Volatility of amorphous solid water. *Journal of Physical Chemistry B*, *122*(43), 10044–10050. https://doi.org/10.1021/acs.jpcb.8b06387

Nachbar, M., Duft, D., & Leisner, T. (2019). The vapor pressure of liquid and solid water phases at conditions relevant to the atmosphere. *The Journal of Chemical Physics*, *151*(6), 064504. https://doi.org/10.1063/1.5100364

Pankine, A. A., & Tamppari, L. K. (2015). Constraints on water vapor vertical distribution at the Phoenix landing site during summer from MGS TES day and night observations. *Icarus*, *252*, 107–120. https://doi.org/10.1016/j.icarus.2015.01.008

Plane, J. M. C., Carrillo-Sanchez, J. D., Mangan, T. P., Crismani, M. M. J., Schneider, N. M., & Määttänen, A. (2018). Meteoric metal chemistry in the Martian atmosphere. *Journal of Geophysical Research: Planets*, *123*(3), 695–707. https://doi.org/10.1002/2017je005510

Plane, J. M. C., Murray, B. J., Chu, X., & Gardner, C. S. (2004). Removal of meteoric iron on polar mesospheric clouds. *Science*, *304*(5669), 426. https://doi.org/10.1126/science.1093236

Playford, H. Y., Whale, T. F., Murray, B. J., Tucker, M. G., & Salzmann, C. G. (2018). Analysis of stacking disorder in ice I using pair distribution functions. *Journal of Applied Crystallography*, *51*(4), 1211–1220. https://doi.org/10.1107/S1600576718009056

Rapp, M., & Lübken, F. J. (2004). Polar mesosphere summer echoes (PMSE): Review of observations and current understanding. *Atmospheric Chemistry and Physics*, *4*(4), 2601–2633. https://doi.org/10.5194/acp-4-2601-2004

Rapp, M., & Thomas, G. E. (2006). Modeling the microphysics of mesospheric ice particles: Assessment of current capabilities and basic sensitivities. *Journal of Atmospheric and Solar-Terrestrial Physics*, *68*(7), 715–744. https://doi.org/10.1016/j.jastp.2005.10.015

Rapp, M., Thomas, G. E., & Baumgarten, G. (2007). Spectral properties of mesospheric ice clouds: Evidence for nonspherical particles. *Journal of Geophysical Research*, *112*(D3). https://doi.org/10.1029/2006jd007322

Russell, J. M., III, Rong, P., Bailey, S. M., Hervig, M. E., & Petelina, S. V. (2010). Relationship between the summer mesopause and polar mesospheric cloud heights. *Journal of Geophysical Research*, *115*(D16). https://doi.org/10.1029/2010JD013852

Salzmann, C. G., & Murray, B. J. (2020). Ice goes fully cubic. *Nature Materials*, *19*(6), 586–587. https://doi.org/10.1038/s41563-020-0696-6

Salzmann, C. G., Radaelli, P. G., Slater, B., & Finney, J. L. (2011). The polymorphism of ice: five unresolved questions. *Physical Chemistry Chemical Physics*, *13*(41), 18468–18480. https://doi.org/10.1039/C1CP21712G

Shilling, J. E., Tolbert, M. A., Toon, O. B., Jensen, E. J., Murray, B. J., & Bertram, A. K. (2006). Measurements of the vapor pressure of cubic ice and their implications for atmospheric ice clouds. *Geophysical Research Letters*, *33*(17). https://doi.org/10.1029/2006gl026671

Smith, R. S., Huang, C., Wong, E. K. L., & Kay, B. D. (1996). Desorption and crystallization kinetics in nanoscale thin films of amorphous water ice. *Surface Science*, *367*(1), L13–L18. https://doi.org/10.1016/S0039-6028(96)00943-0

Thomas, G. E. (1991). Mesospheric clouds and the physics of the mesopause region. *Reviews of Geophysics*, *29*(4), 553–575. https://doi.org/10.1029/91RG01604

Treacy, M. M. J., Newsam, J. M., & Deem, M. W. (1991). A general recursion method for calculating diffracted intensities from crystals containing planar faults. *Proceedings of the Royal Society of London A*, *433*(1889), 499–520. https://doi.org/10.1098/rspa.1991.0062

Turco, R. P., Toon, O. B., Whitten, R. C., & Keesee, R. G. (1983). Venus: Mesospheric hazes of ice, dust, and acid aerosols. *Icarus*, *53*(1), 18–25. https://doi.org/10.1016/0019-1035(83)90017-9

Vincendon, M., Pilorget, C., Gondet, B., Murchie, S., & Bibring, J. P. (2011). New near-IR observations of mesospheric CO_2 and H_2O clouds on Mars. *Journal of Geophysical Research*, *116*. https://doi.org/10.1029/2011je003827

von Zahn, U., & Berger, U. (2003). Persistent ice cloud in the midsummer upper mesosphere at high latitudes: Three-dimensional modeling and cloud interactions with ambient water vapor. *Journal of Geophysical Research*, *108*(D8). https://doi.org/10.1029/2002JD002409

Whiteway, J. A., Komguem, L., Dickinson, C., Cook, C., Illnicki, M., Seabrook, J., et al. (2009). Mars water-ice clouds and precipitation. *Science*, *325*(5936), 68. https://doi.org/10.1126/science.1172344

Wilson, R. J., & Guzewich, S. D. (2014). Influence of water ice clouds on nighttime tropical temperature structure as seen by the Mars Climate Sounder. *Geophysical Research Letters*, *41*(10), 3375–3381. https://doi.org/10.1002/2014gl060086